[4] D. A. Bathker, "Dual frequency dichroic feed performance," in Antennas for Avionics, 26th Meeting of Avionics Panel, pp. 29-1-29-10, June 1974.
[5] T. Y. Otoshi and M. M. Franco, "Dual passband dichroic plate for X-band," JPL Document D-9648, Jet Propulsion Lab. Pasadena, CA, Apr. 15, 1992.
[6] *Reference Data for Radio Engineers*, Fifth ed. New York: Int. Telephone and Telegraph, pp. 4-28–4-29, 1968.
[7] J. R. Pyle and R. J. Angley, "Cutoff wavelengths of waveguide with unusual cross-sections," *IEEE Trans. Microwave Theory Tech.*, vol. MTT-12, no. 3, pp. 556–557, Sept. 1964.
[8] R. W. Beatty, "Insertion loss concepts," *Proc. IEEE*, vol. 52, pp. 663–671, June 1964.
[9] C. T. Stelzried and T. Y. Otoshi, "Radiometric evaluation of antenna-feed component losses," *IEEE Trans. Instrum. Meas.*, vol. IM-18, no. 3, pp. 172–183, Sept.1969.
[10] T. Y. Otoshi and M. M. Franco, "Radiometric tests on wet and dry antenna reflector surface panels," TDA Progress Reprot 42-100, Jet Propulsion Lab., Pasadena, CA, pp. 111–130, Feb. 15, 1990.
[11] C. T. Stelzried, "Operating noise temperature calibrations of low-noise receiving systems," *Microwave J.*, vol. 14, no. 6, pp. 41–46, 48, June 1971.
[12] T. Y. Otoshi, S. R. Stewart, and M. M. Franco, "A portable Ka-band front-end test package for beam-waveguide antenna performance evaluation—Part I: Design and ground tests," TDA Progress Report 42-106, Jet Propulsion Lab., Pasadena, CA, pp. 249–265, Aug. 15, 1991.
[13] T. Y. Otoshi, "Determination of the dissipative loss of a two-port network from noise temperature measurements," TDA Progress Report 42-111, Jet Propulsion Lab., Pasadena, CA, pp. 71–74, Nov. 1992.
[14] A. C. Ludwig, "The definition of cross polarization," *IEEE Trans. Antennas Propagat.*, vol. AP-21, pp. 116–119, Jan. 1973.

Feeding Structure Contribution to Radiation by Patch Antennas with Rectangular Boundaries

Shih-Chang Wu, Nicolaos G. Alexopoulos, and Owen Fordham

***Abstract*—A combination of piecewise sinusoidal-pulse functions (PWS-P) and semi-infinite microstrip (SIM) current expansion functions are used in the full-wave spectral-domain method to analyze microstrip antennas with arbitrary rectangular boundaries. Radiation properties are formulated in the spectral domain to achieve high numerical efficiency. Two types of microstrip antennas, edge-fed rectangular and inset fed patches, have been analyzed and measured. A LRL de-embedding algorithm has been implemented to measure the input impedance of both antennas. The results show good agreement between measurement and calculated data. The radiation patterns from the edge-fed rectangular patch are measured and are compared with the theoretical data. Results show that the current on the feed line can disturb the antenna radiation pattern.**

I. Introduction

Microstrip patch antennas have been analyzed by a variety of methods, such as the cavity model [1], [2], transmission line model [3], finite-difference time-domain method [4], [5], and spectral-domain method [6]. Among them, the spectral-domain method, which is derived from an electric field integral equation and takes into account the radiation and surface wave effects, is considered to be the most rigorous method.

In the spectral-domain method, the unknown current distributions on the microstrip are represented by a set of expansion functions fictitiously. Therefore, the accuracy of the solution highly depends on how close the real microstrip current can be represented by those expansion functions. In [6], the full-wave spectral-domain method was formulated to study the microstripline fed rectangular patch antennas. The patch current was expanded by entire domain modes, which is an efficient way to represent the current on a large rectangular patch but is less capable to track the current in a small region. Nonphysical results for the patch with a direct feed, whose input impedance was depends on the fictitious overlap length [6, figs. 4 and 5], have been observed; and the accurate input impedance of the nonradiating edge fed case [6, fig. 9] has not been able to obtained.

For arbitrarily shaped direct-fed microstrip antennas, the current nearby the feed point is critical to the antenna input impedance. In this study, the full-wave spectral-domain method is formulated similarly to [6]. The accuracy and diversity of the method have been improved by applying a better choice of the expansion functions. The current traveling on the feed line toward the patch edge is represented by a semi-infinite microstrip (SIM) line current. Piecewise sinusoidal-pulse functions (PWS-P) are applied on the patch and in the vicinity of the transition area [7]. This yields a more accurate representation of the current distribution for the nonradiating-edge feed and slot-cut patch antennas.

In addition, the radiated power and radiation patterns, which are antenna parameters concerned by antenna designers, are calculated from the current distribution on the microstrip combined with an appropriate Green's function. These radiation properties are also formulated in the spectral domain.

In this paper, two direct-fed microstrip patch antennas, nonradiating-edge-fed and slot-cut patches, are studied. The sophisticated LRL (line-reflect-line or thru-reflect-line) de-embedding algorithm has been implemented to measure the antenna input impedance. Good agreement between theory and measurements has been observed on both antennas. The radiation pattern of a nonradiating-edge-fed patch antenna was calculated and compared with the measurement. The results show that the radiation from the feed line makes a significant contribution to the cross-polarization radiation pattern.

II. Analysis

A microstrip patch antenna with a direct feed line, as shown in Fig. 1, consists of a rectangular patch and a uniform microstrip feed line. Both the patch and feed line are located on a grounded dielectric substrate, which is characterized by relative permittivity ϵ_r, relative permeability μ_r, and substrate thickness h.

The full-wave spectral-domain solution of this patch antenna is obtained by solving the electric field integral equations of the tangential fields on the microstrip surface [6], [7]. The current on the microstrip is approximately represented by two different types of expansion functions. One is a PWS-P function which is used to expand the current on the patch and a portion of the feed line; the other is a SIM current, which is used to describe the current on the feed line and is extended to infinity. The overlap between the PWS-P currents and the SIM current is the

Manuscript received July 18, 1991; revised June 2, 1992. This work was supported by the U.S. Army under contract DAAL 03-90G-0182.

S.-C. Wu is with the Department of Electrical and Computer Engineering, New Jersey Institute of Technology, Newark, NJ 07102.
N. G. Alexopoulos and O. Fordham are with the Electrical Engineering Department, University of California, Los Angeles, CA 90024.

IEEE Log Number 9202713.

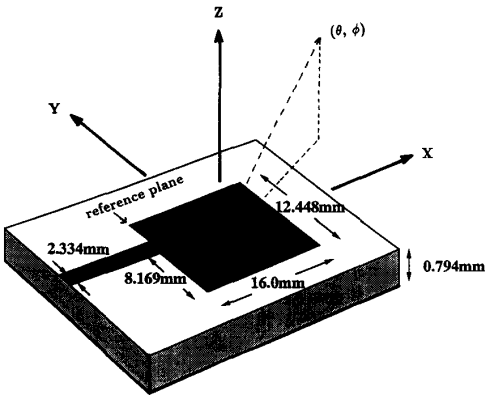

Fig. 1. Dimensions of the edge-fed rectangular patch microstrip antenna.

transition area between a uniformly traveling-wave current and a standing-wave patch current [7].

After the PWS-P and SIM current coefficients are solved, the electromagnetic fields in the upper free space are computed from the these current distribution with the corresponding Hertz potential in the air region. For a given horizontal pseudo-aperture plane ($z = z_0$ plane) located in the air region and infinite in extent, the tangential electric fields, E_x and E_y, can be transformed into $k_x - k_y$ domain. This results in the spectral-domain field expressions of

$$\tilde{E}_x(k_x, k_y, z_0) = \frac{1}{j\omega\epsilon_0\epsilon_r} e^{-q_0(z_0-h)} \cdot \left\{ \left[(k_0^2 - k_x^2)\tilde{J}_x - k_x k_y \tilde{J}_j \right] \frac{\epsilon_r \mu_r \sinh q_1 h}{D_e(k)} - k_x q_0 \left[k_x \tilde{J}_x + k_y \tilde{J}_y \right] \frac{(1 - \epsilon_r \mu_r) \sinh q_1 h \cosh q_1 h}{D_e(k) D_m(k)} \right\} \quad (1)$$

$$\tilde{E}_y(k_x, k_y, z_0) = \frac{1}{j\omega\epsilon_0\epsilon_r} e^{-q_0(z_0-h)} \cdot \left\{ \left[(k_0^2 - k_y^2)\tilde{J}_y - k_x k_y \tilde{J}_x \right] \frac{\epsilon_r \mu_r \sinh q_1 h}{D_e(k)} - k_y q_0 \left[k_x \tilde{J}_x + k_y \tilde{J}_y \right] \frac{(1 - \epsilon_r \mu_r) \sinh q_1 h \cosh q_1 h}{D_e(k) D_m(k)} \right\} \quad (2)$$

$$\tilde{H}_x(k_x, k_y, z_0) = \frac{1}{\epsilon_r} e^{-q_0(z_0-h)} \left\{ q_0 \tilde{J}_y \frac{\epsilon_r \mu_r \sinh q_1 h}{D_e(k)} + k_y \left[k_x \tilde{J}_x + k_y \tilde{J}_y \right] \frac{(1 - \epsilon_r \mu_r) \sinh q_1 h \cosh q_1 h}{D_e(k) D_m(k)} \right\} \quad (3)$$

$$\tilde{H}_y(k_x, k_y, z_0) = -\frac{1}{\epsilon_r} e^{-q_0(z_0-h)} \left\{ q_0 \tilde{J}_x \frac{\epsilon_r \mu_r \sinh q_1 h}{D_e(k)} + k_x \left[k_x \tilde{J}_x + k_y \tilde{J}_y \right] \frac{(1 - \epsilon_r \mu_r) \sinh q_1 h \cosh q_1 h}{D_e(k) D_m(k)} \right\} \quad (4)$$

where

$$D_e(k) = q_0 \mu_r \sinh q_1 h + q_1 \cosh q_1 h \quad (5)$$

$$D_m(k) = q_0 \cosh q_1 h + q_1 \sinh q_1 h / \epsilon_r. \quad (6)$$

A. Radiated Power

Power radiated into the upper half space is calculated by integrating the z component of Poynting's vector over the $z = z_0$ plane. This yields

$$P_{\text{rad}} = \tfrac{1}{2} R_e \left[\int\int E_x H_y^* - E_y H_x^* \, dx\, dy \right]. \quad (7)$$

The asterisk stands for a complex conjugate operator. Applying Parseval's theorem [10], one can transform (7) into $k_x - k_y$ domain as

$$P_{\text{rad}} = \frac{1}{8\pi^2} R_e \left[\int\int \tilde{E}_x \tilde{H}_y^* - \tilde{E}_y \tilde{H}_x^* \, dk_x \, dk_y \right]. \quad (8)$$

From a physical point of view, the electromagnetic wave which propagates into the upper half free space carries away electromagnetic energy and is referred to as the radiated power. By the mathematical expression, these radiated electromagnetic waves are those with a real part in their propagation constant. In the spectral domain, it is equivalent to say that only the waves with a real k_z contribute to the radiated power. It is noted that $k_x^2 + k_y^2 + k_z^2 = k_0^2$, where k_0 is the free space wavenumber. Thus, the integration boundary of (8) can be limited to a circular disk area confined by

$$k_x^2 + k_y^2 \le k_0^2. \quad (9)$$

B. Radiation Pattern

The radiation pattern from a microstrip, including the feed line, is calculated in this subsection. On the $z = z_0$ plane, the equivalent magnetic currents can be defined by Schelkunoff's equivalence principle. These equivalent magnetic currents radiated into free space achieve the same radiation pattern as that radiated by the original microstrip. The far fields are the Fourier transform of these equivalent magnetic currents. The final form of the radiation pattern can be expressed as follows:

$$E_\theta(\theta, \phi) = \cos\phi \tilde{E}_x(k_x, k_y, z_0) + \sin\phi \tilde{E}_y(k_x, k_y, z_0) \quad (10)$$

$$E_\phi(\theta, \phi) = \cos\theta \left[\sin\phi \tilde{E}_x(k_x, k_y, z_0) - \cos\phi \tilde{E}_y(k_x, k_y, z_0) \right]. \quad (11)$$

The functions, $\tilde{E}_x$ and $\tilde{E}_y$, are given in (1) and (2) with the arguments of $k_x = k_0 \sin\theta \cos\phi$ and $k_y = k_0 \sin\theta \sin\phi$, where (θ, ϕ) is the observation angle. Note that there is no integration involved in (10) and (11); the ultimate numerical efficiency is achieved.

III. Measurements and Results

In this study, an edge-fed rectangular patch and an inset-fed patch were analyzed by the method described above. The reflection coefficients of both antennas and radiation patterns of the edge-fed rectangular patch were measured to verify the theoretical results.

A *Wiltron 360* vector network analyzer with coaxial test ports was used to measure the reflection coefficients of the antennas. The coaxial-microstrip transitions typically form radical discontinuities in the propagating fields and produce reflection and loss that increase with frequency. However, most of these degrading effects were removed from the measurements with the LRL de-embedding algorithm [11].

Coaxial-microstrip transitions and LRL standards were fabricated with the same microstrip geometry and dielectric as that of the antenna feed line. The de-embedding was not perfect because the LRL algorithm assumes that the dominant microstrip mode is the only signal path through the transitions and standards. When coupling between coaxial apertures occurs or surface waves are launched in the dielectric layer, these alternate signal paths produce errors which appear as finite return losses for a de-embedded through line.

A. Edge-Fed Rectangular Patch Antenna

The edge-fed rectangular patch antenna is depicted in Fig. 1 and is on a substrate with $\epsilon_r = 2.2$. Its calculated and measured reflection coefficients are compared in Fig. 2. During the theoretical calculation, the x and y directed currents on the patch and the transition area were expanded by 1343 PWS-P functions. The numerical convergence is within 2%. In general, the measurement confirms the theory over the entire frequency band. Fine ripple in the measurement resulted from the transition's reflection interfering with the patch reflection. This ripple was reduced by de-embedding, but was not eliminated because of the alternate signal paths described before.

Several factors produced the small discrepancy between theory and measurement including the dielectric and conductor losses and the deviation of the substrate's dielectric constant from the manufacturer's specification, which was used in the computation. The dielectric and conductor losses, in addition to the radiation and surface wave losses, have reduced the antenna quality factor. As a result, the measured bandwidth at both input-match frequencies is slightly wider than those predicted by theory, which considers only the radiation and surface wave losses. The actual dielectric constant of the substrate, which was used to build the patch antenna, was measured: a large sample was excited as a parallel plate half-wavelength open circuit resonator. Because the ratios of the length and the width to the substrate thickness were so large, the fringing effect was neglected. From the resonant frequency, the measured dielectric constant was determined to be 2.213 instead of the 2.200 used in the numerical computation. The theoretical data was recomputed using this measured substrate dielectric constant at the higher input-match frequency, where a 0.1 GHz discrepancy occurred between theory and measurement. This slight increase in dielectric constant shifted the theoretical input-match frequency from 18.475 GHz ($\epsilon = 2.200$) to 18.39 GHz, while the measured input-match occurred at 18.37 GHz. At 7.6 GHz, which is the first input-match frequency, a 0.3% (23 MHz) frequency shift was expected due to the change in the dielectric constant. Since this shift is beyond the resolution of the plot, the first input-match frequency was not recomputed.

Radiation efficiency of this antenna is defined as the ratio of the radiated power to the input power. At 7.6 GHz, its radiation efficiency is 90.7%, while 7.6% of the input power goes to the surface waves and 1.7% of the power is reflected back to the feed line. The x and y directed current distributions at 7.6 GHz are plotted in Fig. 3. It illustrates that the microstrip line feeds at the nonradiating edge. The x directed current is dominated by the current on the feed line. In this case, we can expect that the current on the transmission line has a major impact on some of the radiation patterns.

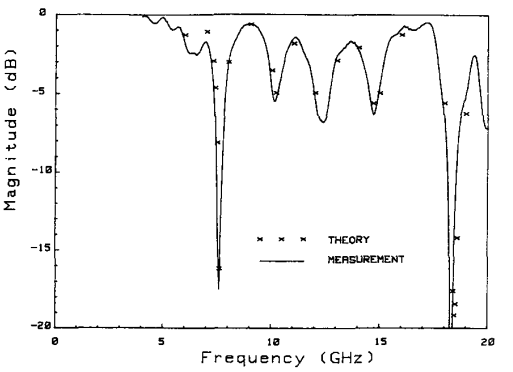

Fig. 2. Reflection-coefficient of the edge-fed rectangular patch microstrip antenna.

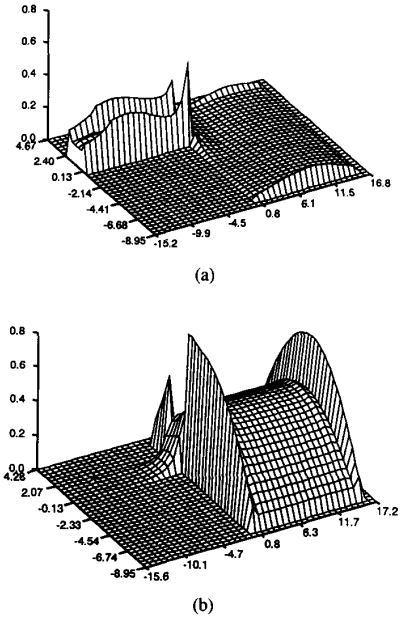

Fig. 3. Current distribution of the edge-fed rectangular patch microstrip antenna at 7.6 GHz. (a) x-directed current. (b) y-directed current.

The radiation patterns of this edge-fed rectangular patch antenna were measured inside the anechoic chamber at UCLA. In Fig. 4, the normalized radiation patterns for both E_θ and E_ϕ on the $\phi = 0°$ and 90° cuts at 7.6 GHz are plotted. The definition of the observation angle (θ, ϕ) is according to the Cartesian coordinates shown in Fig. 1. The solid line in Fig. 4 is the measured pattern from the patch on a 10 in × 10 in substrate (RT/duroid 5880, $\epsilon_r = 2.2$). The dotted line is the theoretical curve which is calculated by (10) and (11) and considers a semi-infinite feed line. The dashed line is the theoretical curve which takes into account the finite length of the feed line, which is measured from the fabricated antenna board and is 4.55 in.

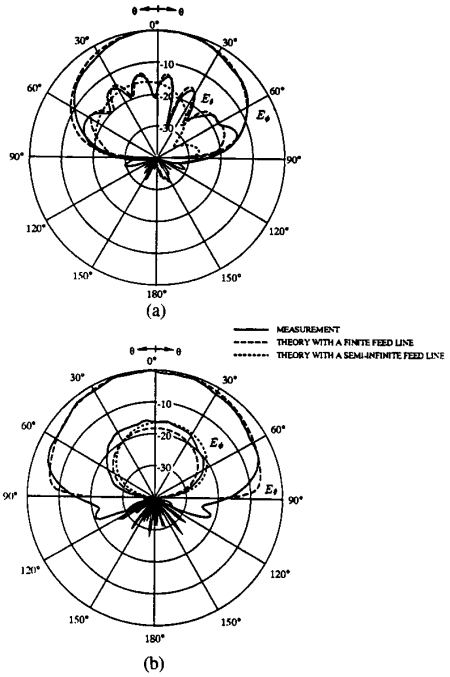

Fig. 4. Radiation pattern of the edge-fed rectangular patch antenna at 7.6 GHz. (a) On 0° degree cut. (b) on 90° degree cut.

During the LRL de-embedding procedure, at 7.6 GHz, the measured magnitude of the S22 of the coaxial-microstrip transition (port #2 is the microstrip port) is 0.036, and the reflection coefficient of the patch antenna is 0.13. Thus, the first high-order reflected current on the microstrip feed line, which is caused by the coaxial-microstrip transition, is −47 dB below the input signal, and can be neglected in the antenna pattern calculation.

In general, the measured data is in good agreement with the theoretical data for the finite-length feed. The comparison of the dashed and the dotted lines in Fig. 4(a) shows a significant effect due to the finite-length feed line on the E_θ component for the $\phi = 0°$ cut. This is because the E_θ component at $\phi = 0°$ is mainly contributed by the x directed current. In addition, the measured patterns in Fig. 4 show that a small fraction of energy is radiated into the rear side, where θ is greater than 90°. This is caused by edge diffraction on the finite ground plane of the measured microstrip patch antenna [12].

B. Inset-Fed Patch Antenna

A patch antenna with an inset feed is widely used in monolithic microstrip phased arrays. A parametric study of a patch antenna with various inset lengths (L shown in Fig. 5) has been performed using the full-wave spectral-domain method. The substrate used in this study is characterized by the relative dielectric constant ϵ_r of 2.33 and the thickness of 62 mils.

The Smith chart in Figure 6 shows the loci of the input impedance versus inset lengths at five different frequencies. The solid lines are the frequency response for a constant inset length. The dashed lines plot the input impedance as a function of the inset length at a constant frequency. In practice, an inset-fed patch antenna is designed to achieve an input match condition. From the input-impedance loci shown in Fig. 6, one

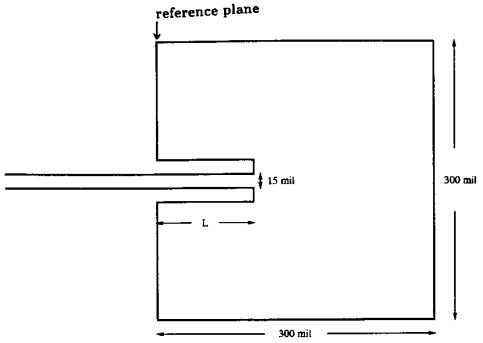

Fig. 5. Dimensions of the inset-fed patch microstrip antenna.

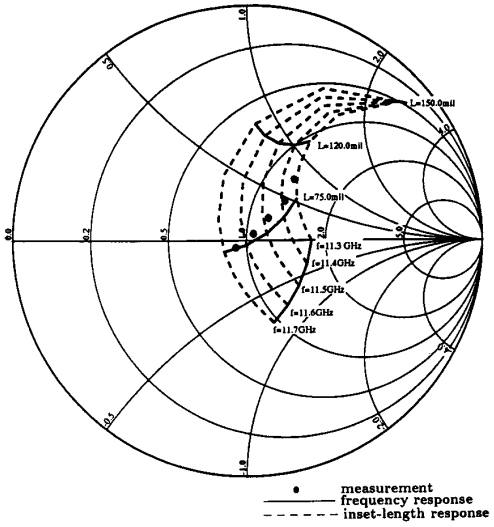

Fig. 6. Input impedance of the inset-fed patch microstrip antenna.

can observe that an input match has been achieved at 11.6 GHz when the inset length is 75 mils. In order to match the dimension of feed line and the slots, 1581 PWS-P functions with the dimension of 15 mils × 7.5 mils were used in the theoretical calculation.

The reflection coefficient of the 75-mil inset-fed patch was measured by the same procedure used for the edge-fed patch. The characteristic impedance of the feed line is about 169 Ω at the frequency of interest. Therefore, the coaxial-microstrip transitions were fabricated with a section of 90 Ω microstrip line to serve as a quarter-wave transformer at the center frequency of 11.5 GHz. The LRL calibration lumped the impedance steps into the S-parameters of the transitions. The solid circles in Fig. 6 are the measured input impedances of this 75-mil inset-fed patch at 11.3, 11.4, 11.5, 11.6, and 11.7 GHz, from right to left. The reflection coefficients agree to within an error vector of magnitude 0.1. The discrepancy may have been caused by the small substrate size (2 in × 2 in) used in the measurement.

By the previous definition of radiation efficiency, this antenna achieves a radiation efficiency of 81.5% at 11.6 GHz. The current distribution of this inset fed patch antenna, under the input match condition, is plotted in Fig. 7. It shows large

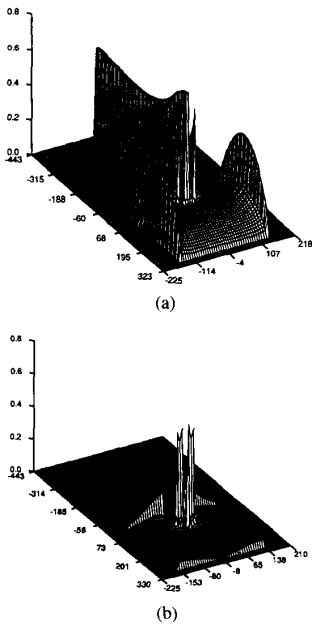

Fig. 7. Current distribution of the patch antenna with an inset length of 75.0 mils at 11.6 GHz. (a) x-directed current. (b) y-directed current.

fluctuation at the junction of the inset feed and the patch. This type of current fluctuation is accurately represented only by a subdomain current expansion function, such as a PWS-P function.

IV. Conclusion

In conclusion, this study has presented an accurate simulator to analyze patch antennas with arbitrary rectangular-shaped boundaries by applying PWS-P functions and SIM currents as microstrip current expansion functions. An efficient method to calculate the radiated power and the far-field pattern based on the spectral-domain analysis is also carried out explicitly. Good agreement has been achieved between theoretical data and measurements. The effect of the feed line length on the cross polarization pattern of a nonradiating edge fed patch antenna has been demonstrated and is substantial.

References

[1] Y. T. Lo, D. Solomon, and W. F. Richards, "Theory and experiment on microstrip antennas," *IEEE Trans. Antennas Propagat.*, vol. AP-27, pp. 137–145, March 1979.

[2] K. R. Carver and J. W. Mink, "Microstrip antenna technology," *IEEE Trans. Antennas Propagat.*, vol. AP-29, pp. 2–24, Jan. 1981.

[3] R. W. Dearnley and R. F. Barel, "A broad-band transmission line model for a rectangular microstrip antenna," *IEEE Trans. Antennas Propagat.*, vol. 37, pp. 6–15, Jan. 1989.

[4] A. Reineix and B. Jecko, "Analysis of microstrip patch antennas using finite difference time domain method," *IEEE Trans. Antennas Propagat.*, vol. 37, pp. 1361–1369, Nov. 1989.

[5] D. M. Sheen, S. M. Ali, M. D. Abouzahra, and J. A. Kong, "Application of the three-dimensional finite-difference time-domain method to the analysis of planar microstrip circuits," *IEEE Trans. Microwave Theory Tech.*, vol. 38, pp. 849–857, July 1990.

[6] D. M. Pozar and S. M. Voda, "A rigorous analysis of a microstripline fed patch antenna," *IEEE Trans. Antennas Propagat.*, vol. 35, pp. 1343–1350, Dec. 1987.

[7] S. C. Wu, H. Y. Yang, N. G. Alexopoulos, and I. Wolff, "A rigorous dispersive characterization of microstrip cross and tee junctions," *IEEE Trans. Microwave Theory Tech.*, vol. 38, pp. 1837–1844, Dec. 1990.

[8] J. R. Mosig and F. E. Gardiol, "General integral equation formulation for microstrip antennas and scatterers," *Proc. Inst. Elec. Eng.* pt. H, vol. 132, pp. 424–432, 1985.

[9] A. Papoulis, *The Fourier Integral and Its Applications*. New York: McGraw-Hill, 1962.

[10] P. M. Morse, *Methods of Theoretical Physics*. New York: McGraw-Hill, 1978.

[11] G. F. Engen and C. A. Hoer, "Thru-reflect-line: An improved technique for calibrating the dual six-port automatic network analyzer," *IEEE Trans. Microwave Theory Tech.*, vol. MTT-27, pp. 987–993, Dec. 1979.

[12] J. Huang, "The finite ground plane effect on the microstrip antenna radiation patterns," *IEEE Trans. Antennas Propagat.*, vol. AP-31, pp. 649–653, July 1983.

Application of the Regularization Method to the Inverse Black Body Radiation Problem

Lixin Dou and R. J. W. Hodgson

Abstract—**The inverse black body radiation problem is concerned with the determination of the area temperature distribution of a black body source from spectral measurements of its radiation. Although several inversion approaches have been developed, none of them has overcome the problem of the ill-posedness. In this study, Tikhonov's regularization method is applied to the solution of the inverse black body radiation problem. A very simple implementation of this approach together with applications of this method are presented. Discussions and conclusions on the effect of the regularization parameter and operator on the results are included.**

I. Introduction

The inverse black body radiation problem is to determine the area temperature distribution of a black body source from power spectral measurements of its radiation. The problem is of interest in a variety of physical experiments and in the remote sensing of chaotic sources. Recently, a lot of attention has been paid to this problem.

The first formulation of the black body problem was proposed by Bojarski [1] in 1982. A numerical solution was presented using the Laplace transform and an iterative process. Following Bojarski's pioneering work, various authors provided different improvements based on his solution [2]–[9]. All these solutions involved the use of the inverse Laplace transform, even the exact closed form solution provided by Kim and Jaggard [8] and the modified Mobius inverse formula provided by Chen [9]. Each of these solutions suffers a defect with regard to implementation with real data.

We have to note that the inverse black body radiation problem is an inherently ill-posed problem [10] (actually it is a Fredholm integral equation of the first kind, which is ill-posed). Converting the original problem into an inverse Laplace transform problem can not help us to get rid of this ill-conditioning.

Manuscript received December 3, 1991; revised May 27, 1992.

The authors are with the Ottawa–Carleton Institute for Physics, University of Ottawa, Ottawa, ON, Canada K1N 9B4.

IEEE Log Number 9202718.